

Stiffness optimisation of graded microstructural configurations using asymptotic analysis and machine learning

Chuang Ma^{a,b}, Dingchuan Xue^c, Shaoshuai Li^{a,b}, Zhengcheng Zhou^{a,b}, Yichao Zhu^{a,b,d,*}, Xu Guo^{a,b,d,*}

^a*State Key Laboratory of Structural Analysis for Industrial Equipment, Department of Engineering Mechanics, Dalian University of Technology, Dalian, 116023, P. R. China*

^b*International Research Center for Computational Mechanics, Dalian University of Technology*

^c*Department of Engineering Science and Mechanics, Pennsylvania State University, University Park, PA 16802, USA*

^d*Ningbo Institute of Dalian University of Technology, No.26 Yucai Road, Jiangbei District, Ningbo, 315016, P. R. China*

Abstract

The article is aimed to address a combinative use of asymptotic analysis and machine learning, for fast stiffness design of configurations infilled with smoothly-varying graded microstructures. The discussion is conducted in the context of an improved asymptotic-homogenisation topology optimisation (AHTO plus) framework (Zhu et al., 2019). It is demonstrated that machine learning can be employed to represent the key but implicit inter-relationships between formulations obtained at different orders from asymptotic analysis. Moreover, in the context of microstructural homogenisation, asymptotic analysis helps offer a platform for machine learning to release its full potentials in function representation. Firstly, asymptotic analysis identifies a computational routine for data acquisition, thus the training data are sufficient in theory. Secondly, the number of input arguments for machine learning can be minimised based on the explicit results by asymptotic analysis, and the scale of the machine learning model in use is kept small. Thirdly, the input arguments for machine learning are shown to be complete. Then the situation where certain factors affecting the function relationship represented by machine learning is avoided. Other issues on incorporating machine learning into the AHTO plus framework, such as ensuring the positive definiteness of the homogenised elasticity tensor and the speeding-up of the associated sensitivity analysis, are also discussed here. Numerical examples show

that the use of machine learning in the AHTO plus scheme can bring about an acceleration by two orders of magnitude, if compared with the existing treatments of using a zoning strategy.

Keywords: Graded microstructural configuration, Machine learning, AHTO plus, Speed up calculation.

1. Introduction

As shown in Fig. 1, lattice augmentation configuration generally refers to the configuration with microstructural cells. Lattice augmentation materials have shown great application potential in mechanics, heat, acoustics and optics[1–6]. In recent years, with the rapid development of 3D printing technology (additive manufacturing), the manufacturing technology of functional equipment and devices with finely designed microstructures has become more and more mature, which naturally promotes the development of corresponding intelligent/automatic design algorithms. In the past few decades, the asymptotic homogenization method has been widely used in the analysis of lattice augmentation configuration due to its perfect mathematical theory, and structural topology optimisation has played an important role in the optimisation design of lattice augmentation configuration.[6–8]

When the basic unit of the augmentation configuration is a specific type of cell structure, it is called the spatial periodic lattice filling structure, and the asymptotic homogenization method provides a mathematical. In 1978, Bensoussan et al.[9]gave the basic mathematical description of the asymptotic homogenization method. It believes that each point of the macroscopic structure is infinitely smaller than the macro and infinitely larger than the micro. There are infinitely many periodic cells at each point. By solving a series of partial differential equations defined on the cells, the equivalent elastic modulus at each point is obtained, and then the structure can be regarded as a continuum and solved by finite element method. Subsequently,

*Corresponding author

Email addresses: yichaozhu@dlut.edu.cn (Yichao Zhu), guoxu@dlut.edu.cn (Xu Guo)



Fig. 1. lattice augmentation configuration

this method was pioneered in the topological optimisation design of spatial periodic structures by Bendsoe and Kichuchi (1989)[10], who realized material redistribution by changing the size and angle of the microstructure within the unit cell. Furthermore, the unit cell microstructure can be replaced by density, and the volume fraction at each point can be minimized to 0 or 1 by penalizing. This method is called solid isotropic material penalizing method (SIMP), which is widely used in the design of various structures. In 1994, O. Sigmund[11] proposed a method of material microstructure design based on the theory of homogenization and topology optimisation, also known as the inverse homogenization method. By using this method, a specific unit cell structure can be obtained that meets certain requirements (such as specific elastic modulus). Based on Sigmund's work, many researchers have done a lot of work in the design of unit cell microstructures, such as the microstructure design of extreme performance materials; piezoelectric material microstructure design; band gap material design; material permeability optimisation, etc. On the basis of previous work, Cheng et al. (2008)[12] This method applies both the micro-scale penalty and the macro-scale penalty (PAMP). The micro unit cell configuration and the macro point density are used as design variables at the same time, and the periodic characteristics of the unit cell are still retained as a whole. This method has been widely applied to more problems, such as parallel multi-scale design[12–14], multi-functional design[15–17], and uncertain loading problem[18], etc.

The above works based on the asymptotic homogenization method provides a cross-scale framework for analyzing the mechanical behavior of periodic microstructures filled with space. However, whether in nature[19–21] or in artificial materials[22–24], a large number of high-performance structures do not meet the space cycle conditions. Compared with the periodic microstructure, the shape of the unit cell of the gradual microstructure changes gradually in space, which has a more degree of design freedom. With the improvement and development of material controllable synthesis preparation, industrial manufacturing technology and practical application requirements, the analysis and design of gradual microstructures have become more and more important. For gradual microstructures, the periodicity assumption of the structure is no longer valid, the traditional asymptotic homogenization theory is no longer applicable, and new configuration description and solution methods are needed.

For the optimisation design of lattice gradual filling structure, it is necessary to study from three aspects: gradual microstructure representation, stress analysis and topology optimisation. By using the level set method, predecessors have conducted a lot of research[25–27], and these works have enriched the characterizable unit cell structure. At the same time, through the improvement of the traditional asymptotic homogenization method, some interesting methods have also been proposed. Zhou and Li [28] Zhou and Li made the unit cell volume fraction and Young’s modulus gradually change in one direction (still a periodic structure along its vertical direction), and designed the gradual microstructure using the inverse-homogenization method. A. Radman et al.[26, 27] also conducted A series of studies in this aspect. The limitations of these methods are mainly reflected in the following three aspects: **(1)** The forming cells are usually rectangular or cuboid, so the spatial changes are only allowed in the direction parallel to the edge of one of the cells (unit cells cannot rotate); **(2)** The smooth connection of cell boundary cannot be guaranteed; **(3)** The accuracy of the calculation results can not be controlled.

Recently, some groundbreaking new methods have been introduced to the design of filled gradient microstructures. These methods not only solve the problem of discontinuity of adjacent cells, but also make the shape of cells no longer limited to rectangular

or cuboid. In addition to directly dividing the finite element mesh on fine scale for calculation, these methods can be roughly divided into three categories: (1)Conformal mapping[29–31]; (2)De-homogenization method[32–34]; (3)Improved asymptotic homogenization method (AHTO plus)[8].

Conformal mapping (Panagiotis et al., 2018) [29–31] uses a level set function to describe its unit cell topology, and uses the conformal characteristic of conformal mapping to ensure that the orthogonality in the basic unit cell structure will not change when it is mapped to a prescribed flow pattern. Because the design function embeds geometric information, it can be directly used in manufacturing. However, when using conformal mapping, a Ricci flow equation must be solved, which is a partial differential equation defined on a prescribed flow pattern and requires steady-state numerical solution. It undoubtedly increases the amount of calculation.

De-homogenization(J.P. Gloen, O.Sigmund, G. Allaire, etc.)[32–34]focuses on the unit cell of the layered structure, and theoretically guarantees the optimality of understanding. By projecting the complex fine-scale periodic structure, it connects the macro and micro scales, and controls the projection topology to achieve topology optimisation on the coarse scale. They first determined the unit cell ratio and direction, and then solved another optimisation problem by projecting the actual microstructure. This method believes that the optimal direction should be consistent with the local principal stress direction. This method guarantees smooth connectivity, but still limits the design freedom of the unit cell.

Zhu et al (2019)[8]proposed a novel rapid IGM design method. This method uses the Movable Deformable Component Method (MMC) for the topology description of IGM, which is an explicit topology optimisation framework that directly contains the geometric information of the unit cell. This is very friendly to general-purpose computer-aided design (CAD) software and is suitable for the design and manufacture of IGM. This method first maps the gradual microstructure in space to a periodic microstructure in virtual space through a continuous mapping function. In this case, the topological description function (TDF) of the IGM structure can be represented by the TDF of the unit cell in the virtual space and the macro mapping function.

This also naturally satisfies the condition of smooth connection between adjacent unit cells. Then the homogenization formula under this description is derived through asymptotic analysis, so that the description of GMC, compliance calculation and topology optimisation are coordinately integrated into the new framework. Compared with the above two methods, the AHTO plus method does not introduce additional calculations, such as the solution of the Ricci flow equation in the conformal mapping and the projection operation in the de-homogenization method. At the same time, the unit cell in the AHTO plus method is no longer limited to a rectangle or a cuboid. It not only allows the unit cell to be rotated, but also allows stretching and shearing, which greatly increases the design freedom of the structure. However, this method still requires finite element solution for the unit cell problem at each point, which still consumes a lot of computational cost. In order to reduce the calculation cost, the linearization operation [8] was used in Zhu et al.’s work in 2019, which effectively reduces the calculation requirements, but also greatly limits the design freedom of IGM. In order to solve this problem, Xue et al. [7, 35] then introduced a zoning scheme, which greatly reduces the calculation. But this method is not accurate enough when there are fewer zones, and increasing zones will bring calculations again.

Through the above description, it can be found that the difficulty of the asymptotic homogenization problem is to find the connection between the macro and micro scales, and this process often requires a huge amount of calculation. It leads to problems such as low efficiency in the calculation of the algorithm, and restricts the application of the algorithm. In this case, the feature that machine learning can fit arbitrary functional relationships and express them explicitly has attracted attention.

In the early days, people’s typical research on machine learning included threshold logic units [36] and perceptrons[37], etc.They laid the foundation for modern neural networks and deep learning, but the machine learning algorithms at that time could only learn linear equations, which had great limitations. In 1970, Linnainmaa proposed a back-propagation model [38]. In 1986, Hinton et al. pioneered the application of error back propagation in neural networks [39], and BP neural network was proposed. Later, Cybenko proved that neural networks containing hidden layers can learn

any equation. This discovery is also known as the Universal Approximation Theorem [40], and this method is widely used in the field of prediction and recognition.

Considering that the macro and micro problems in the AHTO plus method can be completely decoupled, in order to reduce the calculation amount of the AHTO plus method, it is considered that the solution of the unit cell problem and the calculation process of the homogenized elastic modulus to be replaced with a neural network model to avoid the finite element solution to the unit cell problem point by point. Specifically, the Jacobian matrix (corresponding to the conversion of virtual and real space) is randomly generated as input in a certain range, and then it is substituted into the unit cell problem to calculate the homogenised displacement, and then the homogenised elastic properties are obtained as the output. Repeat the process to generate a training database, and use the BP neural network to train the database. After finding a suitable result, replace the corresponding part of the AHTO plus method and apply it to the topology optimisation framework (use difference to obtain sensitivity). This method effectively solves the problem of excessive calculation caused by solving the unit cell problem point by point based on the finite element method in the AHTO plus method. At the same time, for the zoning strategy, this method makes it feasible to divide more zones. Within a certain error range, this method greatly improves the calculation efficiency of the AHTO plus optimisation framework, and provides more accurate and efficient numerical analysis tools for the fine design of various functionally graded materials.

The remaining parts of this article are arranged as follows: In Sec. 2, first briefly introduces the AHTO plus method, and analyzes its advantages and disadvantages. Sec. 3 introduces the neural network model into the AHTO plus method to replace the original unit cell problem solving and equivalent modulus calculation. This part will focus on the method of generating the training database and the process of establishing the network. Sec. 4 proposes the application of coupled machine learning AHTO plus method in the maximum stiffness topology optimisation problem, and gives the sensitivity calculation method. In Sec. 5, the corresponding 2D numerical examples are given, and the calculation results and calculation time of the AHTO plus

method with the zoning strategy are compared to prove the efficiency and accuracy of the method in this paper. Finally, the conclusion and summary of this article are given, and a reasonable outlook is made.

2. The AHTO plus framework

Facing the more diversified design requirements of lattice gradient structure, Zhu et al. (2019) [8] proposed the AHTO plus method by extending the idea of scale separation. Its core module includes the topology description of graded microstructural configuration (GMC), equivalent compliance analysis and topology optimisation. In this section, the key ideas of this method is briefly summerised.

2.1. Topological description of graded microstructures

Given a porous design domain Ω , we use Ω^s to denote the solid region within Ω . Mathematically, Ω^s can be identified by introducing a topology description function $\phi(\mathbf{x})$ defined by:

$$\phi(\mathbf{x}) \begin{cases} \geq 0, & \mathbf{x} \in \Omega^s; \\ < 0, & \mathbf{x} \in \Omega \setminus \Omega^s. \end{cases} \quad (1)$$

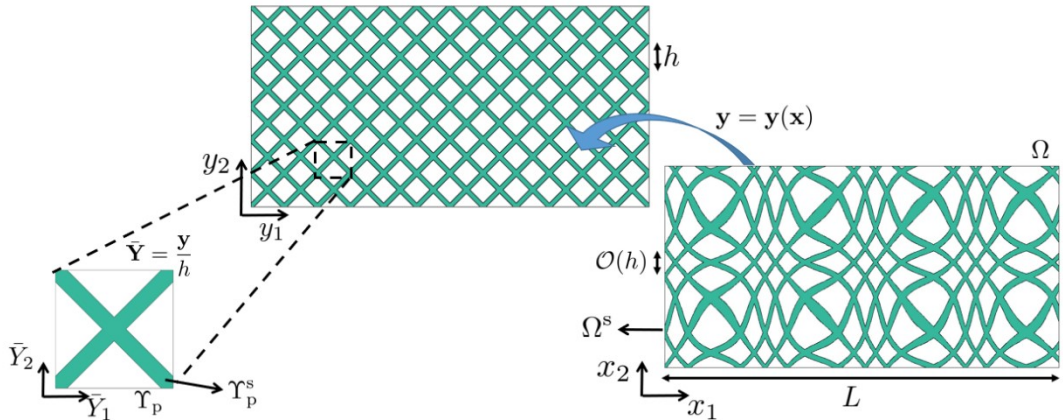


Fig. 2. Generate gradient structure based on compound topology description method (3)

Under the AHTO plus framework, a GMC is generated as follows. As shown in Fig. 2, a continuous mapping function $\mathbf{y} = \mathbf{y}(\mathbf{x})$ is introduced to map a GMC in

real space to a periodic structure in virtual space, which is composed of identical unit cells of size h . Here we introduce

$$\bar{\mathbf{Y}} = \frac{\mathbf{y}(\mathbf{x})}{h}. \quad (2)$$

Here we use $\Upsilon^p = [-1/2, 1/2]^n$ to denote this matrix cell, where n represents the spatial dimension, and the superscript p represents periodicity. Under coordinates $\bar{\mathbf{Y}}$, the micro-scale unit cell as given in the bottom-left panel of Fig. 2, becomes non-dimensional and of unit size. The structure carried by the matrix cell can be described by a microscopic topology description function denoted by $\phi^p(\bar{\mathbf{Y}})$. The TDF of GMC can be expressed by the composition of the macroscopic mapping function $\phi^p(\bar{\mathbf{Y}})$ and the microscopic TDF description function $\phi^p(\cdot)$, i.e.,

$$\phi(\mathbf{x}) = \phi^p\left(\frac{\mathbf{y}(\mathbf{x})}{h}\right). \quad (3)$$

The TDF given by Eq. (3) essentially generates a GMC by filling the design space with deformed matrix cells. The deformation operation includes stretching, rotating and twisting. Mathematically, the actual deformation of the matrix cell in space is controlled by the Jacobian matrix defined by

$$J_{ij} = \frac{\partial y_i}{\partial x_j}. \quad (4)$$

The advantageous features of the composite function (3) have been summarised in existing literature (e.g. [8] [35]). It is worth noting that one can also construct a GMC with more than one matrix cells, and the composite TDF (3) should be modified accordingly (Xue et al. 2020 [7]). The method derived in this article can be generalised to cover such scenarios with ease.

2.2. Scale separation

A GMC is associated with at least two length scales. In this paper, L represents the macro-scale of the design domain, and h represents the micro-scale of the unit cell. In theory, they should satisfy

$$\epsilon = \frac{h}{L} \ll 1. \quad (5)$$

Directly analysing the mechanical properties of a GMC on a fine scale normally renders very high computational cost. It is necessary to introduce an asymptotic homogenization method for speeding the computation up.

The idea is to extend the treatments of scale separation for periodic microstructure. The key difference lying in the case of GMC, is that the homogenised elastic moduli are no longer uniform in space, because of the microstructural variance in space. For greater details about the asymptotic analysis of the GMC behaviours can be found in Zhu et al. 2019 [8]. Here we simply outline the key results.

The homogenised displacement field \mathbf{u}^H satisfies a macroscopic balance equation given by:

$$\frac{\partial}{\partial x_j} \left(\mathbb{C}_{ijkl}^H \frac{\partial u_k^H}{\partial x_l} \right) + f_i^H = 0, \mathbf{x} \in \Omega, \quad (6)$$

where $\mathbb{C}^H = (\mathbb{C}_{ijkl}^H) (i, j, k, l = 1, \dots, n)$ represents the elastic moduli of the equivalent continuum; $\mathbf{f}^H = (f_i^H) (i = 1, \dots, n)$ represents the homogenized body force density. Here we let $\mathbf{f}^H = \mathbf{0}$. The homogenised elastic moduli \mathbb{C}_{ijkl}^H by Eq. (6) are calculated by

$$\mathbb{C}_{ijkl}^H = \mathbb{C}_{ijkl} |\Upsilon_p^s| - \mathbb{C}_{ijst} J_{nt} \int_{\Upsilon_p^s} \frac{\partial \xi_s^{kl}}{\partial \bar{Y}_n} \bar{\mathbf{Y}}, \quad (7)$$

where the third-order tensor $\xi(\bar{\mathbf{Y}}; \mathbf{x}) = (\xi_i^{jk}(\bar{\mathbf{Y}}; \mathbf{x}))$, $i, j, k = 1, \dots, n$ are the generalized displacements, Υ_p^s is volume fraction. The first term on the right side of Eq. (7) measures the homogenised elastic moduli by means of the volume fraction of the matrix cell. The role of the third-order tensor ξ_i^{jk} , $i, j, k = 1, \dots, n$ is then identified. It helps capture the effect due to the materials structure with the unit cell. This third-order tensor is then determined by a set of cell problems governed by

$$J_{mj} \frac{\partial}{\partial \bar{Y}_m} \left(\tilde{\mathbb{C}}_{ijkl} J_{nl} \frac{\partial \xi_k^{st}}{\partial \bar{Y}_n} \right) = J_{mj} \frac{\partial \tilde{\mathbb{C}}_{ijst}}{\partial \bar{Y}_m}, \quad \bar{\mathbf{Y}} \in \Upsilon_p, \quad (8)$$

imposed with periodic boundary condition, and the Jacobian matrix \mathbf{J} is defined by Eq. (4). Compared with conventional asymptotic homogenisation approaches for periodic structures, the homogenised elastic moduli \mathbb{C}_{ijkl}^H are also dependent on the Jacobean matrix \mathbf{J} , which carries the information about how the matrix cell gets deformed at a macroscopic point \mathbf{x} .

2.3. Compliance optimisation and sensitivity analysis

Upon homogenisation, the elastic energy stored in a GMC can be asymptotically calculated by

$$\min_{\mathbf{y}(\mathbf{x}), \phi^p(\bar{\mathbf{Y}})} \varepsilon^H = \frac{1}{2} \min_{\mathbf{y}(\mathbf{x}), \phi^p(\bar{\mathbf{Y}})} \int_{\Omega} \mathbb{C}_{ijkl}^H \frac{\partial u_i^H}{\partial x_j} \frac{\partial u_k^H}{\partial x_l} d\mathbf{x}. \quad (9)$$

For stiffness optimisation, one seeks to minimise the elastic energy of a GMC, where the design variables can be roughly divided into two groups: the macroscopic design variables $d_{\mathbf{x}}$ control the spatial variance of the unit cell and the microscopic design variables d_{β} controlling the material topology within the unit cell.

The optimisation process can be speeded up, if the sensitivities of the design variables to the elastic energy quantity ε are known. As from Xue et al. 2020 [35], we have

$$\frac{\partial \varepsilon^H}{\partial d_{\tau}} = - \int_{\Omega} \frac{\partial \mathbb{C}_{ijkl}^H}{\partial d_{\tau}} \frac{\partial u_i^H}{\partial x_j} \frac{\partial u_k^H}{\partial x_l} d\mathbf{x}. \quad (10)$$

With Eq. (10) the derivatives are taken on the homogenised elastic moduli \mathbb{C}_{ijkl}^H . This is the idea of the adjoint method [41].

The derivatives of the equivalent modulus \mathbb{C}_{ijkl}^H to the macro design variable d_{α} can be expressed as:

$$\frac{\partial \mathbb{C}_{ijkl}^H}{\partial d_{\alpha}} = \frac{\partial \mathbb{C}_{ijkl}^{H[1]}}{\partial d_{\alpha}} + \frac{\partial \mathbb{C}_{ijkl}^{H[2]}}{\partial d_{\alpha}}, \quad (11)$$

where

$$\frac{\partial \mathbb{C}_{ijkl}^{H[1]}}{\partial d_{\alpha}} = - \int_{\Upsilon_p} \left[\frac{\partial J_{nq}}{\partial d_{\phi}} \frac{\partial \xi_p^{ij}}{\partial \bar{Y}_n} \tilde{\mathbb{C}}_{pqkl} + \frac{\partial J_{mt}}{\partial d_{\phi}} \frac{\partial \xi_s^{kl}}{\partial \bar{Y}_m} \tilde{\mathbb{C}}_{ijst} \right] d\bar{\mathbf{Y}}; \quad (12)$$

$$\frac{\partial \mathbb{C}_{ijkl}^{H[2]}}{\partial d_{\alpha}} = \int_{\Upsilon_p} \left[\frac{\partial J_{nq}}{\partial d_{\alpha}} \frac{\partial \xi_p^{ij}}{\partial \bar{Y}_n} \left(\tilde{\mathbb{C}}_{pqst} J_{mt} \frac{\partial \xi_s^{kl}}{\partial \bar{Y}_m} \right) + \frac{\partial J_{mt}}{\partial d_{\alpha}} \frac{\partial \xi_s^{kl}}{\partial \bar{Y}_m} \left(\tilde{\mathbb{C}}_{pqst} J_{nq} \frac{\partial \xi_p^{ij}}{\partial \bar{Y}_n} \right) \right] d\bar{\mathbf{Y}}. \quad (13)$$

The derivatives of the equivalent modulus \mathbb{C}_{ijkl}^H with respect to the micro design variable d_{β} can be expressed as:

$$\frac{\partial \mathbb{C}_{ijkl}^H}{\partial d_{\beta}} = \int_{\Upsilon_p} \left(\delta_{ip} \delta_{jq} - J_{nq} \frac{\partial \xi_p^{ij}}{\partial \bar{Y}_n} \right) \frac{\partial \tilde{\mathbb{C}}_{pqst}}{\partial d_{\beta}} \left(\delta_{ks} \delta_{lt} - J_{mt} \frac{\partial \xi_s^{kl}}{\partial \bar{Y}_m} \right) d\bar{\mathbf{Y}}, \quad (14)$$

where $\delta_{ij}, i, j = 1, \dots, n$ is Kronecker symbol.

2.4. Major challenge

As the microstructure varies in space now, the homogenised elastic moduli become heterogeneous in the effective continuum. Consequently, one may need to solve the cell problem (8) as many times as the number of the finite elements for solving the homogenised problem. To address this issue, schemes of linearisation ([8]) and zoning ([35], [7]) were proposed in separate. But either the design freedom is sacrificed or computational burden for the cell problem (8) is still considerable. Facing with this challenge issue, the present article considers employing machine learning to fully release the potentials of the AHTO plus method, and the effectiveness of such a combinative use of asymptotic analysis and machine learning is then demonstrated with numerical examples in Sec. 4.

3. Neural network representation of homogenised elastic moduli

The homogenised elastic moduli \mathbb{C}_{ijkl}^H , as from Eq. (7), calculated only with the knowledge of the third-order tensor ξ_i^{jk} , and this is the sole reason for the introduction of the cell, problem (8). And Eq. (8) implies that ξ_i^{jk} are actually determined by the Jacobean \mathbf{J} and the topology of the matrix cell carried by the TDF $\phi^p(\cdot)$. This indicates an implicit function relation between \mathbb{C}_{ijkl}^H and these two sets of variables, i.e.,

$$\mathbb{C}_{ijkl}^H = \mathbb{C}_{ijkl}^H(\mathbf{J}, \phi^p(\bar{\mathbf{Y}})). \quad (15)$$

In this section, we seek to use machine learning to identify this implicit, but fully determined function relationship (15).

3.1. Neural network input and output

Before applying machine learning, one needs to clearly declare the inputs and outputs setting a neural network up. Here the identification of inputs and outputs is conducted with following two criteria. Firstly, the inputs and outputs should all be non-dimensional and normalised. This is good for determining the ranges for data generation. Secondly, the number of inputs should be minimised. So as to keep neural

network’s complexity low. This is done by exploring the inter-relationship among the input arguments. Thirdly and occasionally, certain key properties carried by the output arguments can not be preserved automatically by neural networks. Hence one may need to adjust the corresponding output argument to argument to maintain the desired properties. We still soon see an example, where the homogenised elasticity tensor should be positively defined.

3.1.1. Non-dimensionalisation

Note that the expected inputs of Eq. (15), \mathbf{J} and the parameters of $\phi^p(\bar{\mathbf{Y}})$, are already non-dimensionalised. Here the ranges for \mathbf{J} and the parameters of $\phi^p(\bar{\mathbf{Y}})$ are quite “normal”. This is because a too large component in \mathbf{J} may result in severe distortion of the matrix cell, which should be avoided during optimisation. Moreover, $\phi^p(\bar{\mathbf{Y}})$ is defined in a cell χ^p of unit size. Thus the parameters it carries should take “normal” values.

Hence one just considers the non-dimensionalisation of the output of Eq. (15), \mathbb{C}_{ijkl}^H , which is naturally carried out by

$$\bar{\mathbb{C}}_{ijkl}^H = \frac{\mathbb{C}_{ijkl}^H}{E}, \quad (16)$$

where E is Young’s modulus. Note that a bar is a top of a variable, to indicate that it is defined through non-dimensionalisation.

3.1.2. Dimension reduction for input arguments

The inputs of Eq. (15) are from two sources: the spatially-varying deformation of the matrix cell measured by \mathbf{J} and the materials structure with the matrix cell controlled by the coefficients of $\phi^p(\cdot)$. To do dimension reduction for \mathbf{J} , we refer to Appendix 1, where the (non-dimensional) homogenised tensor is found to be independent of $\det \mathbf{J}$, the determinant of \mathbf{J} . Hence the actual (macroscopic) inputs can be chosen to be \mathbf{J}' , where

$$\det \mathbf{J}' = 1. \quad (17)$$

For an arbitrary \mathbf{J} , when calling the trained neural network, one simply rescales

it by

$$J'_{ij} = (\det \mathbf{J})^{-\frac{1}{n}} J_{ij} \quad (18)$$

for use.

As for the microscopic TDF $\phi^p(\cdot)$, there are many ways to represent it. Here the MMC framework. This is because as an explicit way of describing structural topology, the MMC framework has fewer number of design variables, if compared with other implicit topology optimisation approaches.

3.1.3. Positive definiteness of the homogenised elasticity tensor

The (non-dimensional) homogenised tensor $\bar{\mathbb{C}}^H$ is shown to bear symmetry as follows (Zhu et al. [8])

$$\bar{\mathbb{C}}^H_{ijkl} = \bar{\mathbb{C}}^H_{jikl} = \bar{\mathbb{C}}^H_{klij}, \quad \text{for } i, j, k, l = 1, \dots, N. \quad (19)$$

With such symmetry, the number of outputs can be reduced from n^4 to $(\frac{(n+1)n}{2} + 1)\frac{(n+1)n}{4}$.

Besides, it is also positively defined, i.e. for any second-order tensor ϵ_{ij} , it satisfies

$$\bar{\mathbb{C}}^H_{ijkl} \epsilon_{ij} \epsilon_{kl} > 0, \quad (20)$$

provided that $\epsilon_{ij} \epsilon_{ij} \neq 0$.

Note that such positive definiteness of \mathbb{C}^H can not be guaranteed when the corresponding neural networks are trained. To ensure such positive definiteness, we re-arrange the fourth-order tensor \mathbb{C}^H_{ijkl} as a symmetric matrix \mathbf{C} . This is done by merging i and j , and k with l , i.e. $\bar{\mathbb{C}}^H_{ijkl} = \mathbf{C}_{IK}$, with $I, K = 1, 2, \dots, \frac{n(n+1)}{2}$, and the matrix \mathbf{C} should be symmetric and positively defined.

Now we apply Cholesky decomposition [42] to the matrix \mathbf{C} , i.e.,

$$\bar{\mathbf{C}} = \mathbf{L}\mathbf{L}^T, \quad (21)$$

where \mathbf{L} is an $\frac{n(n+1)}{2}$ – by $-\frac{n(n+1)}{2}$ lower-triangular matrix, and \mathbf{L}^T denotes the transpose of \mathbf{L} . Then instead of \mathbb{C}^H , one may seek to determine the transpose of \mathbf{L} . Then

instead of \mathbb{C}^H , one may seek to determine the interrelationship between \mathbf{L} and the input arguments, and the (non-dimensional) homogenised elasticity tensor is calculated by Eq. (21).

3.1.4. A brief summary

What we expect from machine learning is a neural network representing the interrelationship of

$$\mathbf{L}_{IK} = \mathbf{Z}_{IK}(\mathbf{J}'; d_1, \dots, d_\beta), \quad (22)$$

where $I \geq K$ and $I, K = 1, \dots, \frac{n(n+1)}{2}$; $\det \mathbf{J}' = 1$; d_1, \dots, d_β are the parameters of the microscopic TDF $\phi^p(\cdot)$ defined in the matrix cell Υ_p .

3.2. Data generation

3.2.1. General produce

Data are needed for training the neural network to represent Eq. (22). Now the input and output arguments have been identified, and the asymptotic homogenisation results ensure that complete determination of the outputs by the input arguments. Then one may take the following steps to generate data training.

Step 1. Evaluation of the input arguments.

First, values are assigned to all the input arguments \mathbf{J}' and d_1, \dots, d_β . Note that if \mathbf{J} is generated arbitrarily, Eq. (18) is used to ensure $\det \mathbf{J}' = 1$. Also note that the effective range for each input argument should be specified in advance. This issue will be further illustrated with a two-dimensional example.

Step 2. Calculation of the resulting cell problem

Evaluating J_{ij} in Eq. (8) by the evaluated J'_{ij} from the previous step, the governing equation for the microscopic problem is ready. Inserting the evaluated microscopic parameters d_1, \dots, d_β into the TDF $\phi^p(\cdot)$, the active domain of definition for the cell problem is identified. Then with periodic boundary conditions imposed, the third-order tensor ξ_i^{jk} can be solved for out of the cell problem.

Step 3. Calculation of the homogenised elasticity tensor.

Using Eq. (7), the (non-dimensional) homogenised elasticity tensor can be evaluated.

Step 4. Application of Cholesky decomposition.

Finally, Cholesky decomposition (21) is applied to the calculated $\bar{\mathbf{C}}^H$ or equivalently, the $\frac{n(n+1)}{2}$ – by $-\frac{n(n+1)}{2}$ matrix $\bar{\mathbf{C}}$ based on Eq. (22). Then a lower matrix \mathbf{L} is obtained, which are the corresponding output values.

Thus a data point is obtained in the multi-dimensional space spanned by the input and output arguments. The process can be repeated (in parallel) to generate more data points.

3.2.2. Two-dimensional examples

A more detailed example on date generation is given with $n = 2$, where the design domain is two-dimensional inspace.

Here the evaluation of \mathbf{J}' is emphasised. In theory, one may randomly assign four values to a 2– by –2 matrix, say, \mathbf{J} , and then calculate \mathbf{J}' with Eq. (18). But the geometric information implied by \mathbf{J}' is fully missing. Alternatively, we can use four other parameters in space of \mathbf{J} . It is noted that in two-dimensional situations, the Jacobean matrix \mathbf{J} should correspond to a parallelogram configuration, which results from the deformation of the unit cell, as shown in Fig. 3. The parallelogram can be characterised by four parameters bearing geometrical meaning: the lengths of two edges λ_1 and λ_2 , a rational angle θ_1 and an interior angle θ_2 . Since the expansion of the parallelogram does not change the corresponding homogenised elasticity tensor, we simply let $\lambda_1 = 1$, and $\lambda_2 = \lambda$.

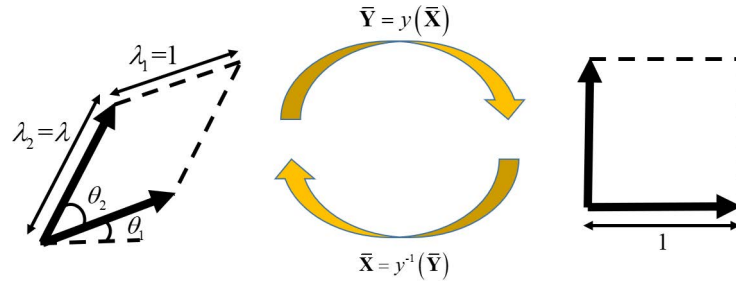


Fig. 3. The mapping function converts a parallelogram unit cell to a square unit cell

Following the derivation by [8], the Jacobean matrix \mathbf{J} identifying the parallelo-

gram in Fig. 3 is formulated by

$$\mathbf{J} = \frac{1}{\lambda \sin \theta_2} \begin{pmatrix} \lambda \sin(\theta_1 + \theta_2) & -\lambda \cos(\theta_1 + \theta_2) \\ -\sin \theta_1 & \cos \theta_1 \end{pmatrix}. \quad (23)$$

Therefore, the evaluation of \mathbf{J} can be done as follows. We first randomly assign certain values to the three geometrical parameters λ, θ_1 and θ_2 . Then we can evaluate \mathbf{J} through Eq. (23). And the values of \mathbf{J}' are finally obtained with the use of Eq. (18).

Such way of evaluating \mathbf{J}' is good for keeping their values with a reasonable range. As discussed above, highly distorted cell is not expected for acuted design. Geometric representation of a deformed matrix cell offers a way to expliciting control its shape. Here are simply lets

$$\frac{1}{\lambda_{\max}} \leq \lambda \leq \lambda_{\max}, \quad 0 \leq \theta_1 < 2\pi, \quad \theta_{\min} \leq \theta_2 \leq \pi - \theta_{\min}, \quad (24)$$

when assigning values to \mathbf{J} .

Here Low Discrepancy Sequence are introduced in order to make the generated data cover the entire design space more evenly ([43]). Commonly used Low Discrepancy Sequence include Radical Inversion, Van der Corput, Halton, Sobol sequences and so on. Among them, the Sobol sequence can directly use bit operation to achieve radical inversion, which is very efficient and is widely used in the fields of graphics, rendering, and finance. In this work, Sobol sequence is used to generate random sequence in 3-dimensional space (λ, θ_1 and θ_2). Then according to Eq. (23) to find the corresponding \mathbf{J} . And normalize the determinant according to Eq. (18) to get \mathbf{J}' as the input variable of the neural network.

For data generation here, we set the matrix cell to be a “X” - shape of volume fraction 30%. Hence the microscopic parameters d_1, \dots, d_β in Eq. (22) are fixed, and the number of active input variables is three, i.e., three of the components of \mathbf{J}' . Then following the procedure detailed in Sec. 3.2.1, 4000 data points are generated both for Eq. (22). Note that although 4000 data points do not sound many for machine learning. But it is shown by the accuracy examples in Sec. 5 that the trained NNs are

sufficiently accuracy for two-dimensional stiffness optimisation with only macroscopic design variables.

3.3. Machine learning

The backpropagation (BP) neural network is a classic machine learning algorithm, and has seen its successful applications in various occasions. The NN represents the relationship (22). As the matrix cell configuration has been fixed, we only have \mathbf{J}' as the input arguments for the NN. The input values are transited to the outputs across several hidden layers.

3.3.1. NN training results

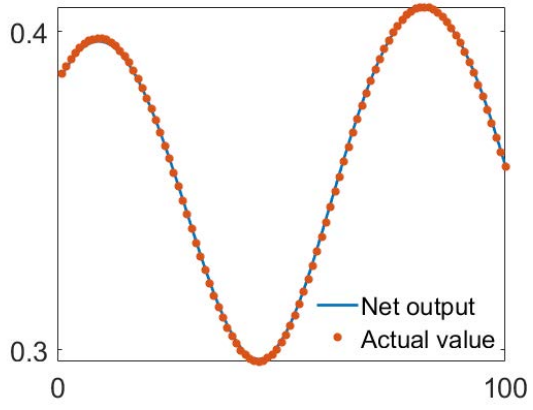
The fully connected neural network is used to train the data. The specific parameters of the network are shown in the following table:

Table 1. Fully connected feedforward neural network parameters list

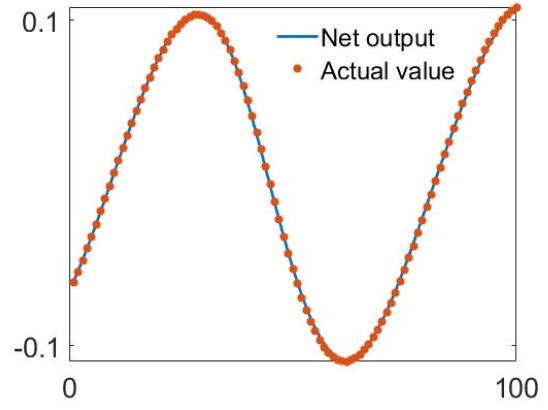
Parameter	Value/Method
Training function	LM training function
Activation function	Sigmoid
Maximum number of training	1000
Learning efficiency	0.01
Target mean square error	0

In order to show the effect of network training, the rotational symmetry of the unit cell structure is tested here. We fix the values of λ and θ_2 , generate 100 sets of θ_1 equidistant between 0-pi, and generate the corresponding 100 sets of homogenization modulus \mathbb{C}_{ijkl}^H according to the steps in Sec. 3.2.1. Furthermore, using our trained network can obtain the fitting effect diagram of 6 homogenised modulus as shown in Fig. 4.

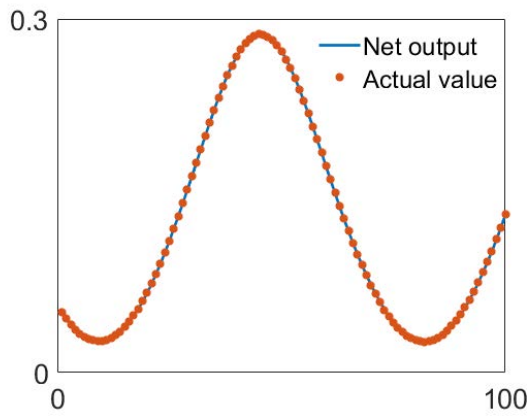
It can be seen from Fig. 4 that the trained neural network function is accurate and smooth, so we can use differential sensitivity instead of analytical sensitivity, which can also speed up the calculation.



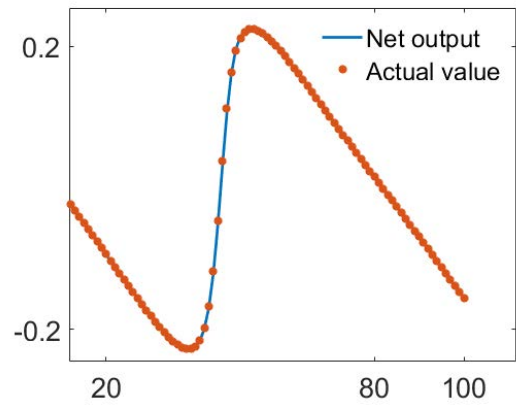
(a) Net1 test (rmse=0.062%)



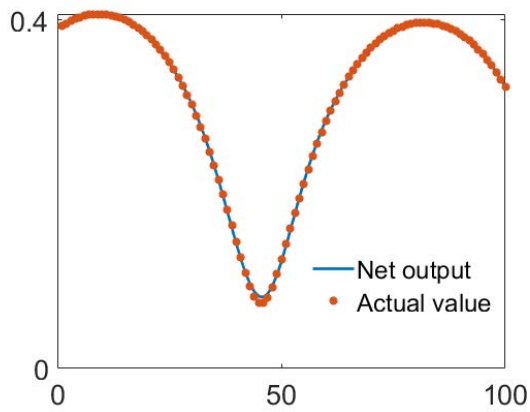
(e) Net4 test (rmse=0.12%)



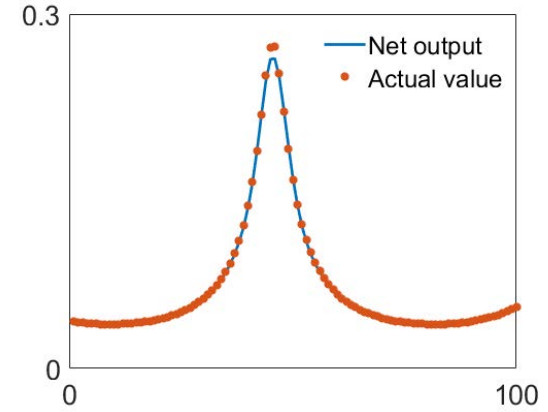
(b) Net2 test (rmse=0.034%)



(f) Net5 test (rmse=0.15%)



(c) Net3 test (rmse=0.18%)



(g) Net6 test (rmse=0.15%)

Fig. 4. Fitting effect diagram of 6 homogenised modulis

4. Stiffness optimisation of GMC

Up to now, the formulation with a combinative use of asymptotic analysis and machine learning is derived. In this section, we discuss the critical issues on implementing it for the stiff optimisation of GMC. This partially the reason of bringing the so-called projection method in other optimisation frameworks about GMC ([33]).

4.1. Design variables

As stated above, design variables for GMC can be divided into two categories. One type is the control parameter of the macro mapping function $\mathbf{y}(\mathbf{x})$, which can also be reflected only in the Jacobian matrix J . The other type is microscopic design variable, which are reflected from the topology description function $\phi^p(\cdot)$ defined on the generating unit Υ_p . Because this article mainly examines the macro-gradient features of GMC, and we fixed the generated unit cell to be the “X” type shown in the lower left corner of Fig. 2. Therefore, the corresponding stiffness optimisation problem has no sensitivity to microscopic design variables.

It is worth pointing out that we may express macroscopic design variables in two ways. One is through the algebraic method, that is, the parameterized expression of the mapping function $\mathbf{y}(\mathbf{x})$. The corresponding design variable is the control parameters of \mathbf{y} . The other is in a geometric manner, where θ_1, θ_2 and λ shown in Fig. 3 are adopted for optimisation. Although it is more intuitive to describe the design variables in a geometric manner, it challenges exist due to the following reasons.

From Eq. (23), we can obtain the values of \mathbf{J} given θ_1, θ_2 and λ . Since \mathbf{J} is derived by taking a partial derivative of \mathbf{y} , it is not easy to calculate \mathbf{y} from \mathbf{J} points, as certain full differential conditions must be met. It should be noted that the inter-relation among θ_1, θ_2 and λ is generally non-analytic, except for special circumstances (for example, in two-dimensional cases where $\mathbf{y}(\mathbf{x})$ is a conformal mapping [34]). This poses great difficulties in reproducing $\mathbf{y}(\mathbf{x})$, which is needed to produce the resulting GMC. Therefore, although not intuitive enough, this article still uses the parameters of $\mathbf{y}(\mathbf{x})$ as macroscopic design variables.

The mapping function $\mathbf{y}(\mathbf{x})$ can be parameterised in the following form:

$$\mathbf{y}(\mathbf{x}) = \sum_{\tau=1}^K h_{\tau} \phi_{\tau}(\mathbf{x}), \quad (25)$$

where $\phi_{\tau}(\mathbf{x})$ represents a series of basis functions, $\tau = 1, \dots, K$; h_{τ} is the corresponding coefficient. Therefore, the mapping function can be expressed in a fully displayed form. And the spatial change is completely determined by a finite number of parameters h_{τ} .

As stated above, the unit cell structure in the virtual space is fixed. The topology of the macrostructure is controlled by the mapping function $\mathbf{y} = \mathbf{y}(\mathbf{x})$, and the design of the microstructure can adopt classic methods, such as SIMP method, level set method, etc. However, if the unit cell shape changes too much, it is not easy to manufacture. Therefore, this paper only considers the optimisation of macroscopic design variables, that is, the control parameters of the mapping function. At the same time, the microstructure parameters are kept unchanged and expressed by the Moving Morphable Components (MMC) method.

Specifically, the polynomial mapping function is used as follows:

$$y_i = a_{ij}x_j + \frac{1}{2}b_{ijk}x_jx_k + \frac{1}{3}c_{ijkl}x_jx_kx_l, \quad (26)$$

$i = 1, \dots, n$. Symmetry: $b_{ijk} = b_{ikj}$, $c_{ijkl} = c_{ijlk} = c_{ilkj} = c_{iklj}$. From $J_{ik} = \partial y_i / \partial x_k$, the Jacobian is expressed as follows:

$$J_{ij}(\mathbf{x}) = a_{ij} + b_{ijk}x_k + c_{ijkl}x_kx_l, \quad (27)$$

$i, j = 1, \dots, n$. So far, the design variables obtained for the optimisation of the macroscopic problem are a_{ij} , b_{ijk} and c_{ijkl} . We use the MMA method as an optimizer for overall topology optimisation. When using polynomials as the mapping function, there are only 18 design variables for the 2D problem. This is conducive to the optimisation of the macro design. However, because the polynomial function is related to the coordinate, the mapping function at the larger coordinate makes the unit cell change beyond the limit. See 5 for details.

In summary, a filled-gradient microstructure can be directly generated by Eq. (25) and the fixed and unchanging unit cell configuration in the virtual space. Only the macro design variables need to be optimised.

4.2. Constraints

It is worth pointing out that considering that the training space of the machine learning model only contains data within the range given by Eq. (24). Thus, we need to restrict the values of θ_2 and λ shown in Fig. 3. From the results of Example 2 in Sec. 5, it is easier for θ_2 to violate the constraints specified by Eq. (24). Therefore, we have tighter requirements on the value range of θ_2 , that is, $\theta_2 \in (\frac{\pi}{4}, \frac{3\pi}{4})$. In addition, $\lambda \in (\frac{1}{3}, 3)$ is required. The above conditions are equivalent to:

$$\frac{1}{9} \leq \lambda^2 \leq 9, \quad \sin(\theta_2) \geq \frac{\sqrt{2}}{2}, \quad (28)$$

As mentioned in Sec. 4.1, the real design variables are $\mathbf{y}(\mathbf{x})$ or the corresponding parameters of \mathbf{J} . In particular, it can be read from Eq. (23) that

$$\lambda^2 = \frac{J_{11}^2 + J_{12}^2}{J_{21}^2 + J_{22}^2}, \quad \sin(\theta_2) = \frac{J_{11}J_{22} - J_{12}J_{21}}{\sqrt{J_{11}^2 + J_{12}^2}\sqrt{J_{21}^2 + J_{22}^2}}. \quad (29)$$

This means that the constraints given by Eq. (28) are implicit for the design variables. We adopt p -norm constraint method. For this we introduce:

$$f_1 = \text{H} \left[\left[\int_{\Omega} \left(\lambda^{2p} + \frac{1}{\lambda^{2p}} \right) d\mathbf{x} \right]^{\frac{1}{p}} - 9 \right], \quad (30a)$$

$$f_2 = \text{H} \left[\left[\int_{\Omega} \left(\frac{1}{\sin \theta_2} \right)^p d\mathbf{x} \right]^{\frac{1}{p}} - \sqrt{2} \right], \quad (30b)$$

where $\text{H}(\cdot)$ is the Heaviside function satisfying

$$\text{H}(t) = \begin{cases} 1, & t > 0; \\ 0, & \text{otherwise} . \end{cases} \quad (31)$$

Besides, as we know that

$$\lim_{p \rightarrow \infty} \left[\int_{\Omega} \left(\lambda^{2p} + \frac{1}{\lambda^{2p}} \right) d\mathbf{x} \right]^{\frac{1}{p}} = \max_{\mathbf{x} \in R} \left[\max \left(\lambda^2, \frac{1}{\lambda^2} \right) \right]. \quad (32)$$

If Eq. (28) holds, the input of the Heaviside function in Eq. (30a) is negative. Then $f_1 = 0$. Thus does f_2 for the second inequality of Eq. (28). For optimisation, the constraints are integrated within the target function, which large numbers multiplied by f_1 and f_2 .

4.3. The optimisation formulation

In summary, the optimisation problem can be described as follows:

$$\begin{aligned}
& \text{Find } \mathbf{y} = \mathbf{y}(\mathbf{x}) \in \mathcal{U}_y, \phi(\bar{\mathbf{Y}}) \in \mathcal{U}(\mathbf{Y}_p) \\
& \text{Minimise } \mathcal{F} = \int_{\Omega^I} \mathbb{C}_{ijkl}^H \frac{\partial u_i^H}{\partial x_j} \frac{\partial u_k^H}{\partial x_l} d\mathbf{x} + K_1 f_1 + K_2 f_2 \\
& \int_{\Omega} \mathbb{C}_{ijkl}^H u_{i,j} v_{k,l} d\mathbf{x} = \int_{\Omega} f_i^H v_i d\mathbf{x} + \int_{\Gamma_t} t_i v_i dS \\
& \forall \mathbf{v} \in \mathcal{U}_{ad} \\
& \mathbb{C}_{ijkl}^H = E \mathbf{L} \mathbf{L}^T, I = 1, \dots, N \\
& \mathbf{L} = \mathbf{Z}(\mathbf{J}'(\mathbf{x})), I = 1, \dots, N; \\
& \mathbf{u}^H = \bar{\mathbf{u}}, \quad \text{on } \Gamma_u \\
& V_f \leq \bar{V}
\end{aligned} \tag{33}$$

where \mathbf{v} is the virtual displacement field, \mathcal{U}_y and $\mathcal{U}(\mathbf{Y}_p)$ are the macro mapping function space and the micro topological description function space, respectively; K_1, K_2 are two larger constants; f_1 and f_2 are given by Eqs. (30a) and (30b); the function $\mathbf{Z}(\cdot)$ is the neural network function, and \mathbf{L} is the lower triangular matrix obtained by Cholesky decomposition.

4.4. Sensitivity analysis

According to the derivation of the sensitivity calculation formula in Sec. 2.3, the sensitivity calculation is mainly $\frac{\partial \mathbb{C}_{ijkl}^H}{\partial d_\gamma}$. Because the microscopic parameters d_1, \dots, d_β in Eq. (22) are fixed, only $\frac{\partial \mathbb{C}_{ijkl}^H}{\partial d_\alpha}$ need to be calculated. According to Sec. 3.3.1, it can be proved that the neural network function is smooth and stable, so here we use differential sensitivity instead of analytical sensitivity.

By Chain Rule,

$$\frac{\partial \mathbb{C}_{ijkl}^H}{\partial d_\gamma} = \frac{\partial \mathbb{C}_{ijkl}^H}{\partial J'_{pq}} \frac{\partial J'_{pq}}{\partial d_\gamma}, \tag{34}$$

where $\mathbf{d} = (d_1, \dots, d_\lambda)^T$ contains all design variables, and $\partial \mathbb{C}_{ijkl}^H / \partial J'_{pq}$ can be obtained by central difference, namely

$$\frac{\partial \mathbb{C}_{ijkl}^H}{\partial J'_{pq}} \approx \frac{\mathbb{C}_{ijkl}^H(\mathbf{J}'|_{J'_{pq} + \Delta J_{pq}}) - \mathbb{C}_{ijkl}^H(\mathbf{J}'|_{J'_{pq} - \Delta J_{pq}})}{2\Delta J_{pq}}. \quad (35)$$

Therefore, the sensitivity of the overall objective function can be expressed as:

$$\frac{\partial \mathcal{F}}{\partial d_\gamma} = \frac{\partial \mathcal{C}^H}{\partial d_\gamma} + K_1 \frac{\partial f_1}{\partial d_\gamma} + K_2 \frac{\partial f_2}{\partial d_\gamma}. \quad (36)$$

4.5. Numerical implementation

The following describes the numerical implementation process of the algorithm in this paper. As shown in Fig. 5, the idea of zoning is adopted, dividing the entire design domain into N zones. After obtaining the equivalent modulus of each zone, the finite element method is used to calculate the homogenized displacement field in the whole area. Furthermore, the equivalent flexibility of each zone is calculated separately, and the overall flexibility is the sum of the flexibility values of each zone.

First, we give the initial value of the design variable \mathbf{d} . Then divide the design domain into N zones as shown in Fig. 5. Each subregion has a corresponding Jacobian matrix $\mathbf{J}^I = \mathbf{J}^I(\mathbf{x})$. Normalize these Jacobian matrices according to Eq. (18), and get the Jacobian matrix of each zone after normalization: $\mathbf{J}'^I = \mathbf{J}'^I(\mathbf{x})$. Xue et al. (2020) [35] have proved that for two-dimensional problems, when each partition includes no more than 25 finite elements, the accuracy of the flexibility calculation can be guaranteed. The flexibility after partition can be expressed as follows:

$$\varepsilon = \sum_{I=1}^N \int_{\Omega^I} \mathbb{C}_{ijkl}^H \frac{\partial u_i^H}{\partial x_j} \frac{\partial u_k^H}{\partial x_l} d\mathbf{x}, \quad (37)$$

the constraints are:

$$\begin{aligned} f_1 &= H \left(\left((\lambda_1^2)^p + (\lambda_2^2)^p + \dots + (\lambda_N^2)^p + \left(\frac{1}{\lambda_1^2} \right)^p + \left(\frac{1}{\lambda_2^2} \right)^p + \dots + \left(\frac{1}{\lambda_N^2} \right)^p \right)^{\frac{1}{p}} - 9 \right), \\ f_2 &= H \left(\left(\left(\frac{1}{\sin(\theta_1)} \right)^p + \left(\frac{1}{\sin(\theta_2)} \right)^p \right) + \dots + \left(\frac{1}{\sin(\theta_N)} \right)^p \right)^{\frac{1}{p}} - \sqrt{2} \right). \end{aligned} \quad (38)$$

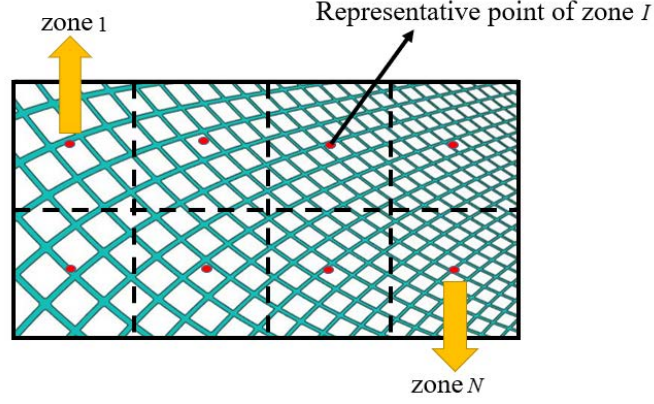


Fig. 5. zone division

Numerical examples show that the optimisation process of present method is very stable. Even if the constraints are not applied, the optimisation result will not exceed the training space of the network.

In order to speed up the calculation, the parallel characteristics of the neural network itself can be used. Combine the \mathbf{J}'^I of each subregion into an input matrix \mathbf{J}' :

$$\mathbf{J}' = \begin{bmatrix} J_{11}^1 J_{11}'^2 & J_{11}^I & J_{11}^N \\ J_{21}^1 J_{11}'^2 & J_{21}^I & J_{21}^N \\ J_{12}^1 J_{11}'^2 & J_{12}^I & J_{12}^N \\ J_{22}^1 J_{11}'^2 & J_{22}^I & J_{22}^N \end{bmatrix} = \{\mathbf{J}'^1, \mathbf{J}'^2, \dots, \mathbf{J}'^N\}, \quad (39)$$

Substitute \mathbf{J}' directly into the machine learning model for calculation. At the same time, output the lower triangular matrix \mathbf{J}' from the elastic matrix decomposition corresponding to each zone:

$$\mathbf{L} = \{\mathbf{L}^1, \mathbf{L}^2, \dots, \mathbf{L}^N\}, \quad (40)$$

Then use NN model to calculate the homogenised elastic modulus \mathbb{C}_{ijkl}^I for each sub-region. Then they are assembled into a macroscopic overall stiffness matrix. Substitute into the macro balance equation (6) and use the finite element method to solve it. We get the uniform displacement field \mathbf{u}^H . Furthermore, the objective function value F corresponding to this configuration is obtained from Eq. (33). Then through sensitivity analysis (36), combined with MMA optimisation method to

update all design variables. Repeat the above process until the convergence condition is met.

4.6. Flowchart

The flowchart of present algorithm numerical implementation is shown as Fig. 6.

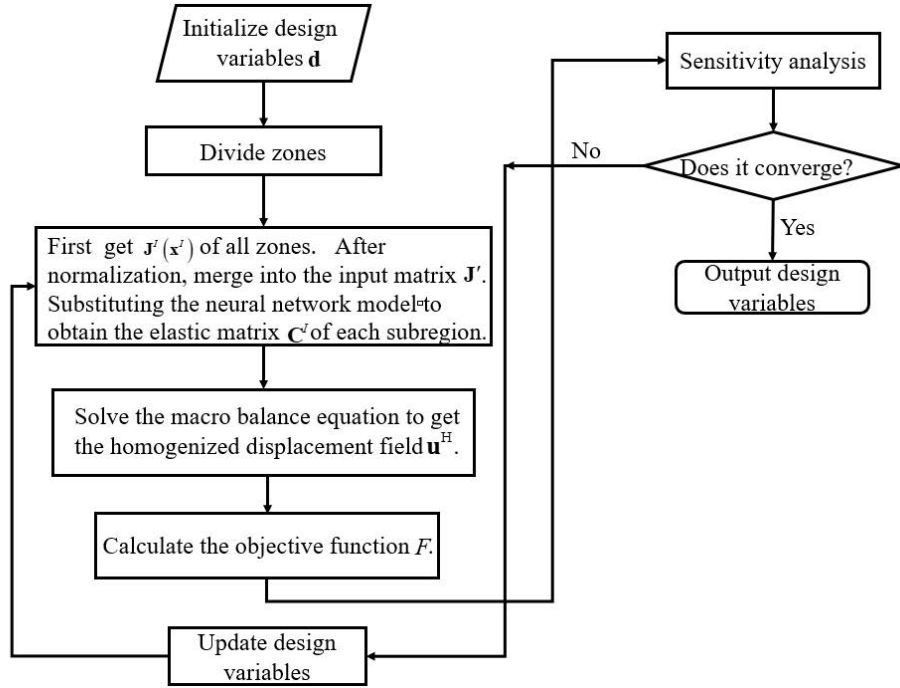


Fig. 6. Optimization flow chart

5. Numerical examples and analysis

In this section, use the methods described in this article to complete two 2D numerical examples. After that, compare the optimisation results of the numerical example with the optimisation results of the original zoning strategy to analyze its accuracy. And further compare the calculation time of the two methods to prove the efficiency of the combined machine learning method.

Next, in order to verify the accuracy and efficiency of the AHTO plus method combined with the machine learning model in this article, a short beam as shown in Fig. 7 is established. And apply uniform load and concentrated load on the upper and

left sides respectively to design and optimize the short beam microstructure. Finally, the advantages and disadvantages of this method are explained by comparing with the existing methods.

5.1. Optimal design of short beam with uniform load on the top

Now consider a short beam with a uniform load on the top, as shown in Fig. 7. The short beam is fixed on the right side, and a uniformly distributed load with an amplitude of 2 is distributed on the upper side. The design domain size is 2×1 . [35] divides the design domain into 16×8 zones at most, and proves that it has converged to the exact solution. Therefore, this article continues the zoning strategy and divides more sub-areas. Consider dividing the design domain into 100×50 sub-regions, and take the center point of each sub-region as the representative point. The volume ratio of solid materials to the entire space is set to 30%. Take the unit cell configuration in the virtual space as shown on the left side of Fig. 8. Then optimize the design domain according to the optimisation process in Fig. 6.

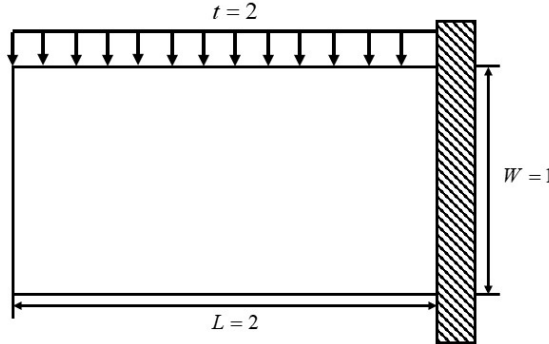


Fig. 7. Schematic diagram of uniformly distributed load above cantilever short beam

After the optimisation of this algorithm, an optimised result with a flexibility value of 739.2 can be obtained, and its configuration is shown in Fig. 8. Compared with the 852.5 optimised result using the zoning strategy (the number of sub-regions is 16×8), the flexibility decreases by 13.3%. In order to verify the accuracy of this optimisation result, a fine grid (1600×800) is directly divided into the entire design domain. To facilitate loading, take $1/200$ of the beam as the solid structure. The calculated result is 704.8. For the sake of comparison, we also take $1/200$ of the beam

as the solid material, and get the compliance value 710.6. The error between the result of present algorithm and the result of the fine calculation is -0.83% , indicating that the optimisation result of the present method converges to the exact solution. At the same time, the calculation efficiency is greatly improved. The decrease in flexibility value during the optimisation process is shown in Fig. 9. Compared with the purely spatial periodic microstructure in the initial state, the optimised microfiber transmits the uniformly distributed load from the top to the right fixed end along a more reasonable force transmission path, which effectively improves the overall rigidity of the structure.

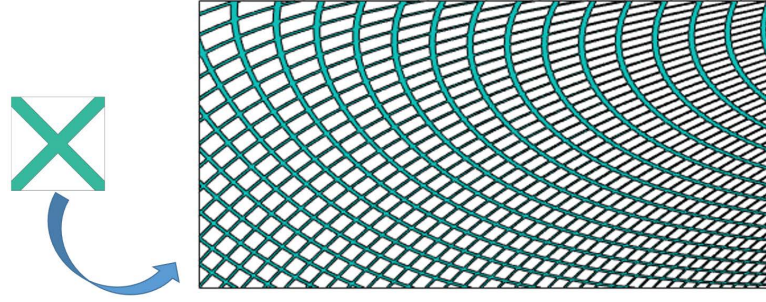


Fig. 8. Optimization result graph

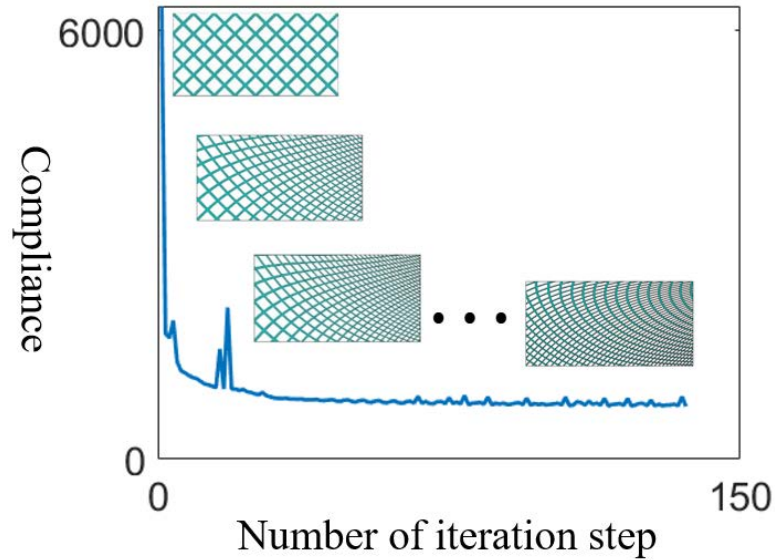


Fig. 9. Flexibility reduction graph

5.2. Optimal design of short beam with concentrated load at the left midpoint

Now consider the case where the left midpoint of the short beam is subjected to a concentrated load as shown in Fig. 10. The design domain size is the same as in Example 1. The unit cell configuration in the virtual space still uses the **X** configuration shown on the left side of the Fig. 8. Using the AHTO plus optimisation method combined with machine learning introduced in this article, the flexibility value of the optimisation result obtained is 273.4. Compared with the 282.6 optimised result using the zoning strategy (the number of sub-regions is 16×8), the flexibility decreases by 3.3%. By taking 1/200 of the beam as the solid structure, the compliance value of the present method is 252.3. Compared with the fine calculation result 255.0, the error is 1.1%. The final configuration is shown in Fig. 11, and the process of flexibility reduction is shown in Fig. 12.

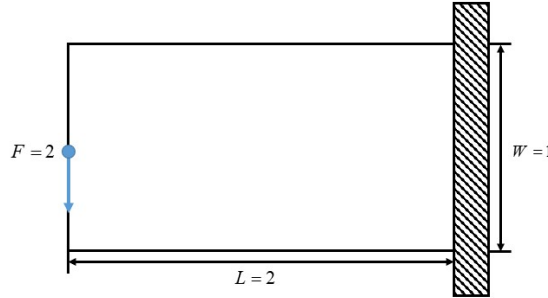


Fig. 10. Schematic diagram of the concentrated load at the left midpoint of the cantilever short beam

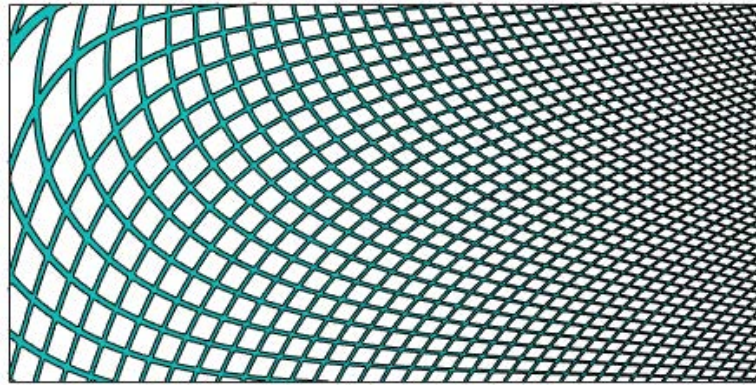


Fig. 11. Optimization result graph

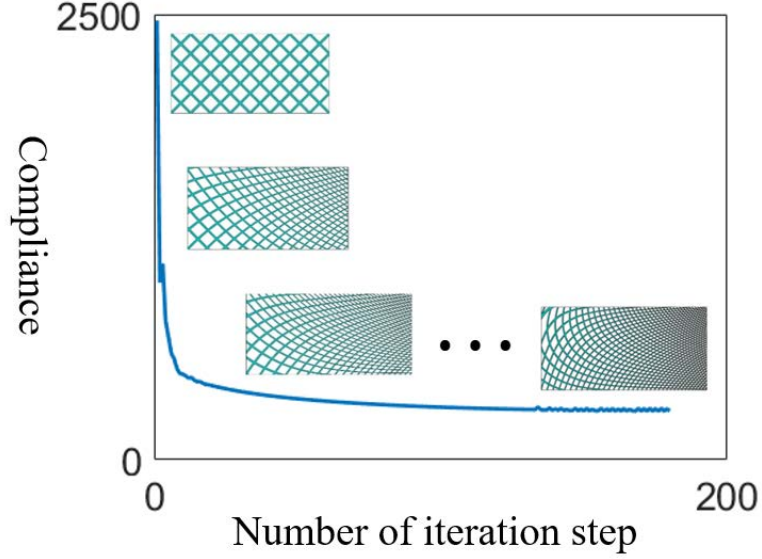


Fig. 12. Flexibility reduction graph

From the two calculation examples above, we can find that the differential sensitivity is more conducive to the optimisation algorithm to jump out of the local optimal solution, so the present algorithm can find better optimisation results than the original algorithm. In addition, the increase in computational efficiency allows more zones to be divided, which is also conducive to the search for the optimisation result. At the same time, computational efficiency has been greatly improved.

5.3. Calculation efficiency comparison

In the following, we will discuss the improvement of calculation efficiency by the present method. The implementation process of the present algorithm has been given above. The calculation efficiency comparison table between the present method and zoning strategy is shown here:

From Table 2, it can be seen that the present method greatly improves the computational efficiency compared to the original zoning strategy. For the case of 128 (16×8) zones, our method (1 core computing) saves 99.8% of time compared to the original zoning strategy of 1 core computing. Compared with the original zoning strategy using 4 cores, it saves 96.9% of time. The increase in computational efficiency makes it possible to divide more sub-areas. From Table 2, it can be seen

Table 2. Calculation efficiency comparison table

Number of zones	Zoning strategy	Zoning strategy	Present algorithm
	(1 core)(s)	(4 cores)(s)	(1 core)(s)
2	13.93	4.15	0.910
8	32.91	4.90	0.897
32	118.95	9.99	0.940
128	459.88	32.75	0.986
5000	/	/	3.436

that even if the number of zones reaches 5000 (100×50), the calculation time is still only 10.5% of the original zoning strategy of 128 zones using 4 cores. It can be seen that the present method can improve the computational efficiency by two orders of magnitude. This superiority makes this method have great application potential in larger scale or three-dimensional problems.

6. Summary

In this article, an optimisation scheme incorporating machine learning into the AHTO plus framework is proposed, so as to accelerate the mechanical behavior analysis and design of filled gradient microstructures. This algorithm effectively solves the problem of excessive calculations caused by the existing AHTO plus method to where the microscopic cell have to be solved for multiple times. Compared with the linearized AHTO plus method, this algorithm increases the designability of the structure and allows the microstructure to have greater deformation in space. Compared with the AHTO plus method that joins the partition strategy, this algorithm makes it possible to divide more zones. And it can ensure that the calculation efficiency is still higher even when more sub-areas are divided. At the same time, the optimisation results are compared with the fine calculation results to prove that the algorithm can guarantee the accuracy of the calculation results within the range of the training space.

The characteristics of the unit cell problem are fully considered when establishing the machine learning model training database. Low Discrepancy Sequence are introduced in order to make the generated data cover the entire design space more evenly. And using Cholesky decomposition enables the machine learning model to train the positive definiteness of the unit cell elastic matrix, ensuring that the output elastic matrix meets the physical meaning of the real situation. Also, the network training space is compressed by normalizing the Jacobian matrix determinant, and the network training effect is improved. In addition, in order to improve the computational efficiency of the network, we can take advantage of the parallel calculation characteristics of the neural network. First obtain the Jacobian matrix \mathbf{J}^I of all zones. Then merge them into an input matrix and input the network together for calculation, and at the same time obtain the output variables of their respective regions. This also improves the computational efficiency of solving the unit cell problem.

From the numerical examples in Sec. 5, it can be seen that the present method greatly improves the computational efficiency and obtains better optimisation results than the original partitioning strategy. This is due to the increase in computational efficiency so that more zones can be divided. In addition, the use of differential sensitivity is also conducive to jumping out of the local optimal solution. This efficient algorithm provides tools for the analysis and design of larger-scale GMC structures and 3D problems.

6.1. Future outlook

The AHTO plus method combined with machine learning model proposed in this paper needs to be improved in the following four aspects.

(1) The selection of the mapping function $\mathbf{y} = \mathbf{y}(\mathbf{x})$ needs to be improved. This article continues the partition strategy, using polynomial functions as mapping functions. The disadvantage is that its design variables are the corresponding polynomial coefficients. The update of the polynomial coefficients has global relevance, that is, the configuration of the local unit cell cannot be adjusted separately. This leads to a larger change in the configuration of the unit cell on the side with a larger coordinate

value (as shown in Figs. 8 and 11. It will exceed the training range of the machine learning model earlier and stop the optimisation of the overall algorithm. To solve this problem, we can consider using b-spline interpolation function and other functions that can adjust the parameters locally without affecting the whole instead of polynomials as a new mapping function in the future.

(2) In the previous numerical examples, it can be seen that the current database is not perfect, and it is not enough to solve more complex optimisation problems. In order to improve the universality of this algorithm, it is necessary to establish a machine learning database with a wider range and containing more unit cell properties. For example, the chiral symmetry and rotational symmetry of the unit cell can be considered to be added to the training database.

(3) In this paper, the difference method is used to calculate the sensitivity of the machine learning part. We can also consider obtaining the corresponding sensitivity by directly deriving the design variables. Another idea is to directly use the sensitivity as the network output to train a new machine learning model. These two solutions need to be tried.

(4) This article currently only uses a fully connected neural network for training. In the future, a special network that is more suitable for fitting partial differential equations can also be considered to further improve the fitting effect of the unit cell problem.

In summary, although the AHTO plus method combined with machine learning model proposed in this paper still has a lot of room for further improvement. But it can be seen that it improves the computational efficiency by two orders of magnitude while ensuring the accuracy of the optimisation results. This makes it a great application prospect in larger-scale design problems or three-dimensional design problems, and provides more accurate and efficient analysis tools for the fine design of various functionally graded materials.

Appendix 1

The following proves that each element in the Jacobian matrix $\tilde{\mathbf{J}}$ is multiplied or divided by a coefficient at the same time, which does not affect its corresponding homogenized elastic modulus \mathbb{C}_{ijkl}^H .

Suppose $J_{ij} = \alpha J'_{ij}$, where α is any constant, substituting it into the unit cell problem governing equation (8) to get:

$$\alpha J'_{mj} \frac{\partial}{\partial \bar{Y}_m} \left(\bar{\mathbb{C}}_{ijkl} \alpha J'_{nl} \frac{\partial \xi_k^{st}}{\partial \bar{Y}_n} \right) = \alpha J'_{mj} \frac{\partial \tilde{\mathbb{C}}_{ijst}}{\partial \bar{Y}_m}, \quad \text{in } \Upsilon_F. \quad (41)$$

Simplified:

$$J'_{mj} \frac{\partial}{\partial \bar{Y}_m} \left(\bar{\mathbb{C}}_{ijk} J'_{nl} \frac{\partial (\alpha \xi_k^{st})}{\partial \bar{Y}_n} \right) = J'_{mj} \frac{\partial \tilde{\mathbb{C}}_{ist}}{\partial \bar{Y}_m}, \quad \text{in } \Upsilon_P. \quad (42)$$

Solve the third-order $\xi_k^{st'} = \alpha \xi_k^{st}$ tensor corresponding to \mathbf{J}' . And substituting the homogenization modulus calculation formula (7) to get:

$$\begin{aligned} \mathbb{C}_{ijkl}^{H'} &= \mathbb{C}_{ijkk} \cdot |\Upsilon_P^s| - \mathbb{C}_{ijst} J'_{nt} \int_{\Upsilon_P} \frac{\partial \xi_s^{kt'}}{\partial \bar{Y}_n} d\bar{\mathbf{Y}} \\ &= \mathbb{C}_{ijkl} \cdot |\Upsilon_P^s| - \mathbb{C}_{ijst} \frac{J_{nt}}{\alpha} \int_{\Upsilon_P} \frac{\partial (\alpha \xi_s^{kt})}{\partial \bar{Y}_n} d\bar{\mathbf{Y}} \\ &= \mathbb{C}_{ijkl} \cdot |\Upsilon_P^s| - \mathbb{C}_{ijst} J_{nt} \int_{\Upsilon_P} \frac{\partial \xi_s^{kt}}{\partial \bar{Y}_n} d\bar{\mathbf{Y}} \\ &= \mathbb{C}_{ijkl}^H, \quad i, j, k, l = 1, \dots, N. \end{aligned} \quad (43)$$

References

- [1] R. Lakes, Materials with structural hierarchy, *Nature* 361 (6412) (1993) 511–515.
- [2] H.-W. Dong, S.-D. Zhao, Y.-S. Wang, C. Zhang, Topology optimization of anisotropic broadband double-negative elastic metamaterials, *Journal of the Mechanics and Physics of Solids* 105 (2017) 54–80.
- [3] O. Sigmund, S. Torquato, Composites with extremal thermal expansion coefficients, *Applied Physics Letters* 69 (21) (1996) 3203–3205.
- [4] M. S. Kushwaha, P. Halevi, L. Dobrzynski, B. Djafari-Rouhani, Acoustic band structure of periodic elastic composites, *Physical review letters* 71 (13) (1993) 2022.
- [5] C. Liu, Z. Du, Z. Sun, H. Gao, X. Guo, Frequency-preserved acoustic diode model with high forward-power-transmission rate, *Physical Review Applied* 3 (6) (2015) 064014.
- [6] N. Aage, E. Andreassen, B. S. Lazarov, O. Sigmund, Giga-voxel computational morphogenesis for structural design, *Nature* 550 (7674) (2017) 84–86.

- [7] D. Xue, Y. Zhu, X. Guo, Generation of smoothly-varying infill configurations from a continuous menu of cell patterns and the asymptotic analysis of its mechanical behaviour, *Computer Methods in Applied Mechanics and Engineering* 366 (2020) 113037.
- [8] Y. Zhu, S. Li, Z. Du, C. Liu, X. Guo, W. Zhang, A novel asymptotic-analysis-based homogenisation approach towards fast design of infill graded microstructures, *Journal of the Mechanics and Physics of Solids* 124 (2019) 612–633.
- [9] G. Papanicolau, A. Bensoussan, J.-L. Lions, *Asymptotic analysis for periodic structures*, Elsevier, 1978.
- [10] M. P. Bendsøe, Optimal shape design as a material distribution problem, *Structural optimization* 1 (4) (1989) 193–202.
- [11] O. Sigmund, Materials with prescribed constitutive parameters: an inverse homogenization problem, *International Journal of Solids and Structures* 31 (17) (1994) 2313–2329.
- [12] L. Liu, J. Yan, G. Cheng, Optimum structure with homogeneous optimum truss-like material, *Computers & Structures* 86 (13-14) (2008) 1417–1425.
- [13] H. Rodrigues, J. M. Guedes, M. Bendsoe, Hierarchical optimization of material and structure, *Structural and Multidisciplinary Optimization* 24 (1) (2002) 1–10.
- [14] P. G. Coelho, P. R. Fernandes, J. M. Guedes, H. C. Rodrigues, A hierarchical model for concurrent material and topology optimisation of three-dimensional structures, *Structural and Multidisciplinary Optimization* 35 (2) (2008) 107–115.
- [15] B. Niu, J. Yan, G. Cheng, Optimum structure with homogeneous optimum cellular material for maximum fundamental frequency, *Structural and Multidisciplinary Optimization* 39 (2) (2009) 115–132.
- [16] J. Yan, X. Guo, G. Cheng, Multi-scale concurrent material and structural design under mechanical and thermal loads, *Computational Mechanics* 57 (3) (2016) 437–446.
- [17] J. Deng, J. Yan, G. Cheng, Multi-objective concurrent topology optimization of thermoelastic structures composed of homogeneous porous material, *Structural and Multidisciplinary Optimization* 47 (4) (2013) 583–597.
- [18] J. Deng, W. Chen, Concurrent topology optimization of multiscale structures with multiple porous materials under random field loading uncertainty, *Structural and Multidisciplinary Optimization* 56 (1) (2017) 1–19.
- [19] C. Sanchez, H. Arribart, M. M. G. Guille, Biomimetism and bioinspiration as tools for the design of innovative materials and systems, *Nature materials* 4 (4) (2005) 277–288.
- [20] P. Fratzl, F. G. Barth, Biomaterial systems for mechanosensing and actuation, *Nature* 462 (7272) (2009) 442–448.
- [21] M. A. Meyers, J. McKittrick, P.-Y. Chen, Structural biological materials: critical mechanics-materials connections, *science* 339 (6121) (2013) 773–779.

- [22] O. Jørgensen, A. Giannakopoulos, S. Suresh, Spherical indentation of composite laminates with controlled gradients in elastic anisotropy, *International journal of solids and structures* 35 (36) (1998) 5097–5113.
- [23] S. Arabnejad Khanoki, D. Pasini, Multiscale design and multiobjective optimization of orthopedic hip implants with functionally graded cellular material, *Journal of biomechanical engineering* 134 (3) (2012).
- [24] Z. Cheng, H. Zhou, Q. Lu, H. Gao, L. Lu, Extra strengthening and work hardening in gradient nanotwinned metals, *Science* 362 (6414) (2018).
- [25] Y. Wang, F. Chen, M. Y. Wang, Concurrent design with connectable graded microstructures, *Computer Methods in Applied Mechanics and Engineering* 317 (2017) 84–101.
- [26] Y. Zhang, M. Xiao, H. Li, L. Gao, S. Chu, Multiscale concurrent topology optimization for cellular structures with multiple microstructures based on ordered simp interpolation, *Computational Materials Science* 155 (2018) 74–91.
- [27] Y. Zhang, H. Li, M. Xiao, L. Gao, S. Chu, J. Zhang, Concurrent topology optimization for cellular structures with nonuniform microstructures based on the kriging metamodel, *Structural and Multidisciplinary Optimization* 59 (4) (2019) 1273–1299.
- [28] S. Zhou, Q. Li, Design of graded two-phase microstructures for tailored elasticity gradients, *Journal of Materials Science* 43 (15) (2008) 5157–5167.
- [29] P. Vogiatzis, M. Ma, S. Chen, X. D. Gu, Computational design and additive manufacturing of periodic conformal metasurfaces by synthesizing topology optimization with conformal mapping, *Computer Methods in Applied Mechanics and Engineering* 328 (2018) 477–497.
- [30] Q. Ye, Y. Guo, S. Chen, N. Lei, X. D. Gu, Topology optimization of conformal structures on manifolds using extended level set methods (x-lsm) and conformal geometry theory, *Computer Methods in Applied Mechanics and Engineering* 344 (2019) 164–185.
- [31] D. Li, W. Liao, N. Dai, Y. M. Xie, Anisotropic design and optimization of conformal gradient lattice structures, *Computer-Aided Design* 119 (2020) 102787.
- [32] J. P. Groen, O. Sigmund, Homogenization-based topology optimization for high-resolution manufacturable microstructures, *International Journal for Numerical Methods in Engineering* 113 (8) (2018) 1148–1163.
- [33] J. P. Groen, J. Wu, O. Sigmund, Homogenization-based stiffness optimization and projection of 2d coated structures with orthotropic infill, *Computer Methods in Applied Mechanics and Engineering* 349 (2019) 722–742.
- [34] G. Allaire, P. Geoffroy-Donders, O. Pantz, Topology optimization of modulated and oriented periodic microstructures by the homogenization method, *Computers & Mathematics with Applications* 78 (7) (2019) 2197–2229.
- [35] D. Xue, Y. Zhu, S. Li, C. Liu, W. Zhang, X. Guo, On speeding up an asymptotic-analysis-

- based homogenisation scheme for designing gradient porous structured materials using a zoning strategy, *Structural and Multidisciplinary Optimization* 62 (2) (2020) 457–473.
- [36] W. S. McCulloch, W. Pitts, A logical calculus of the ideas immanent in nervous activity, *The bulletin of mathematical biophysics* 5 (4) (1943) 115–133.
 - [37] F. Rosenblatt, The perceptron: a probabilistic model for information storage and organization in the brain., *Psychological review* 65 (6) (1958) 386.
 - [38] S. Linnainmaa, The representation of the cumulative rounding error of an algorithm as a taylor expansion of the local rounding errors, Master’s Thesis (in Finnish), Univ. Helsinki (1970) 6–7.
 - [39] G. E. Hinton, T. J. Sejnowski, et al., Learning and relearning in boltzmann machines, *Parallel distributed processing: Explorations in the microstructure of cognition* 1 (282-317) (1986) 2.
 - [40] G. Cybenko, Approximation by superpositions of a sigmoidal function, *Mathematics of control, signals and systems* 2 (4) (1989) 303–314.
 - [41] S. Liu, G. Cheng, Y. Gu, X. Zheng, Mapping method for sensitivity analysis of composite material property, *Structural and multidisciplinary optimization* 24 (3) (2002) 212–217.
 - [42] K. Xu, D. Z. Huang, E. Darve, Learning constitutive relations using symmetric positive definite neural networks, *Journal of Computational Physics* 428 (2021) 110072.
 - [43] S. Mishra, T. K. Rusch, Enhancing accuracy of deep learning algorithms by training with low-discrepancy sequences, *SIAM Journal on Numerical Analysis* 59 (3) (2021) 1811–1834.